

Supporting Information for

High-Performance Oxygen Reduction Electrocatalysts Derived from Uniform Cobalt-Adenine Assemblies

Mengxia Shen^{a,b}, Li-Rong Zheng^c, Wenhui He^a, Changping Ruan^{a,b}, Chunhuan Jiang^a, Kelong Ai^{a,*}, Lehui Lu^{a,*}

^a State Key Laboratory of Electroanalytical Chemistry, Changchun Institute of Applied Chemistry, Chinese Academy of Sciences, Changchun, 130022, P. R. China

^b University of Chinese Academy of Sciences, Beijing, 100039, P. R. China

^c Beijing Synchrotron Radiation Facility, Institute of High Energy Physics, Chinese Academy of Sciences, Beijing, 100049, P. R. China

* The corresponding authors

Email address: klai@ciac.ac.cn; lehuilu@ciac.ac.cn.

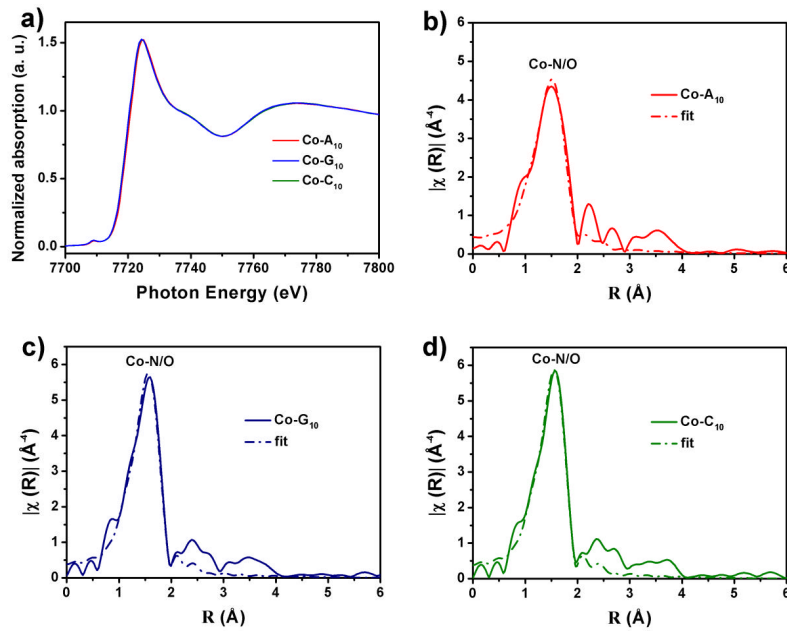


Figure S1. (a) Co K-edge XANES spectra for Co-A₁₀, Co-G₁₀ and Co-C₁₀ NCs. Observed (solid line) and calculated (dash line) Fourier transforms of k^3 -weighted Co K-edge EXAFS spectra for (b) Co-A₁₀, (c) Co-G₁₀ and (d) Co-C₁₀ NCs. XAFS measurements demonstrated that Co atom in Co-A₁₀, Co-G₁₀ and Co-C₁₀ NCs have similar local coordination environments.

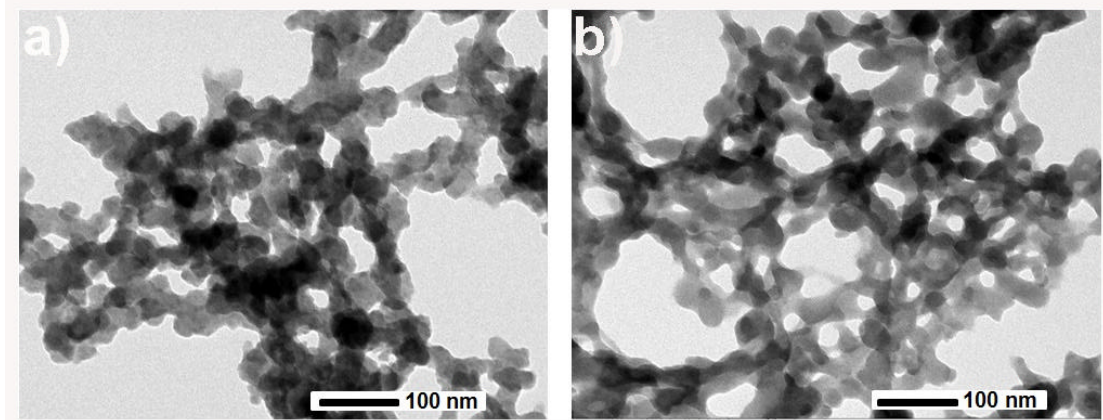


Figure S2. TEM images of (a) Co-G₁₀ and (b) Co-C₁₀ NCs.

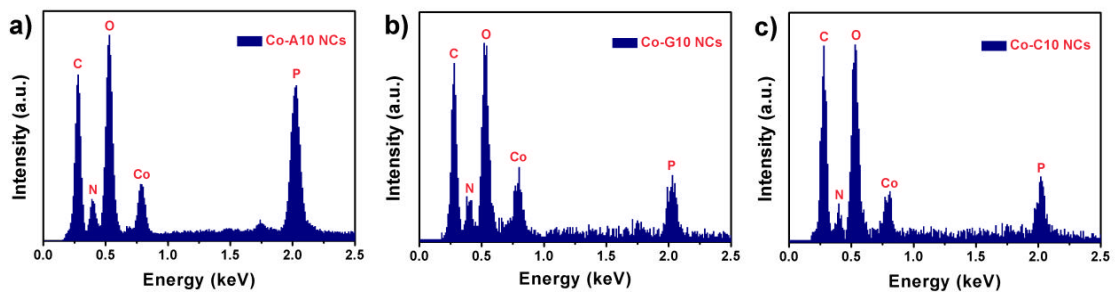


Figure S3. EDX analysis of (a) Co-A₁₀, (b) Co-G₁₀ and (c) Co-C₁₀ NCs.

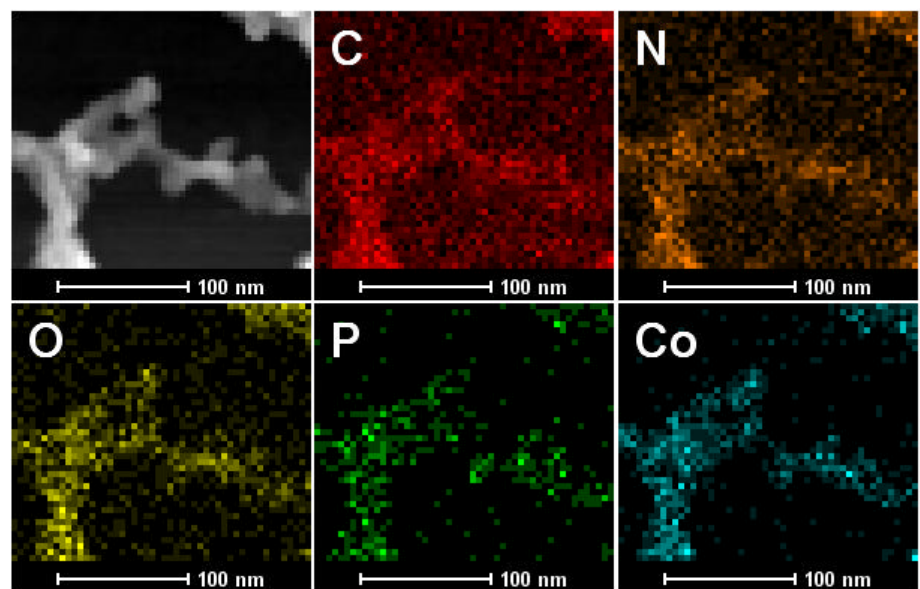


Figure S4. HAADF-STEM maps of Co-A₁₀ NCs, and corresponding elemental mapping images of the well-distribution of C, N, O, P and Co atoms.

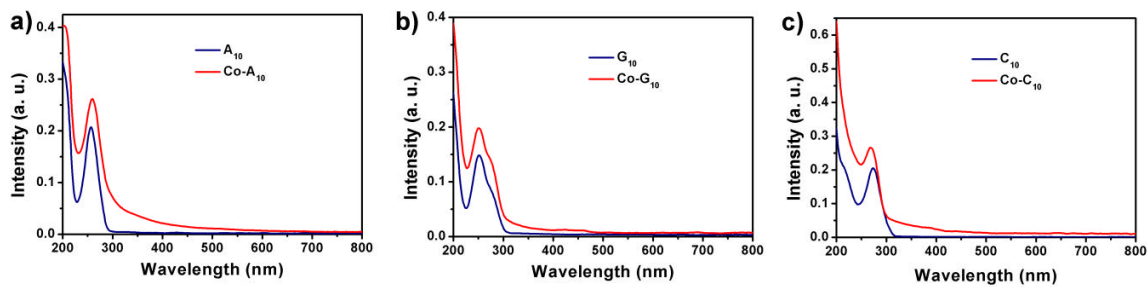


Figure S5. UV-vis absorption spectra of (a) A_{10} , $Co\text{-}A_{10}$, (b) G_{10} , $Co\text{-}G_{10}$ and (c) C_{10} , $Co\text{-}C_{10}$ NCs.

Upon Co(II) complexation, the absorption variation in the UV-vis spectra is observed for all Co-ssDNA conjugation, clearly indicating the chemical coordination and electron coupling between Co(II) and ssDNAs.

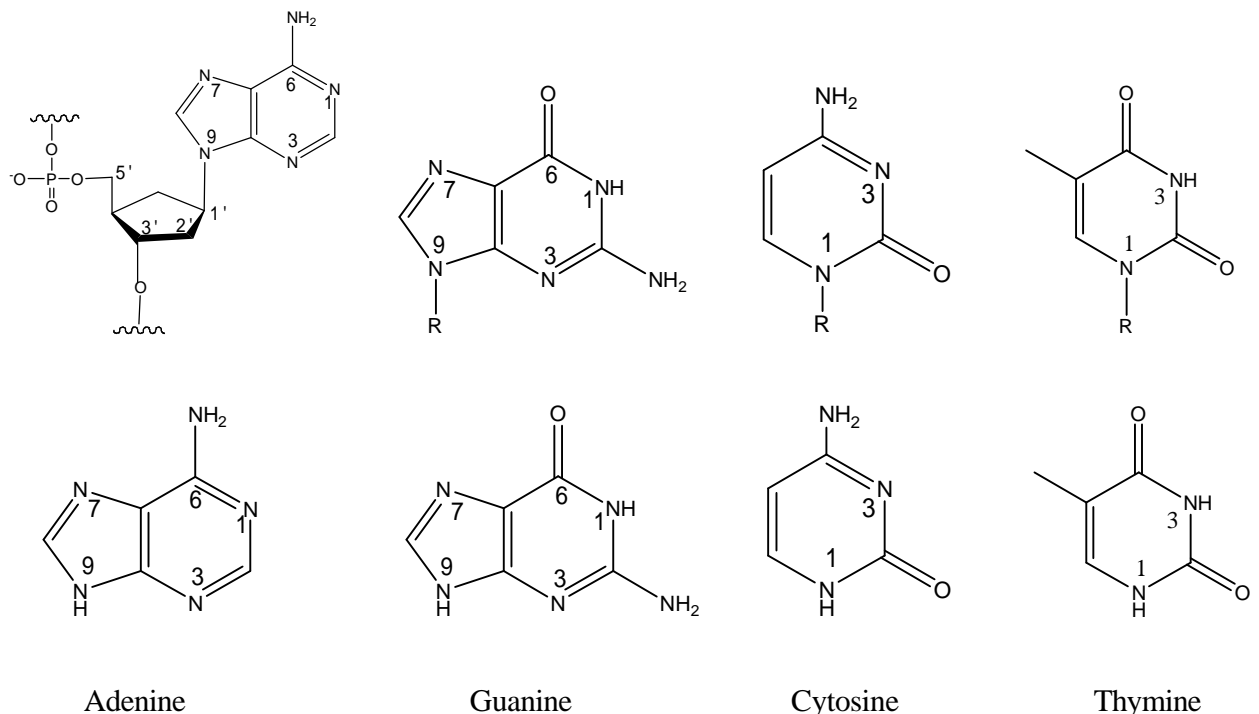


Figure S6. Structures of the ssDNAs (R is phosphate-sugar backbone) and nucleobases (R=H).

(1) The pyridine/imidazole-type nitrogen (N1, N3 and N7) in purine base adenine (A) are efficient metal coordination sites, which lead to the successful formation of Co-A NSs. The calculated coordination number of Co-N/O in Co-A NSs is 4, while this value is increased to 6 in Co-A₁₀. It is therefore concluded that both the pyridine/imidazole-type nitrogen and the phosphate-sugar backbone contribute to the formation of Co-A₁₀.

(2) The pyridine/imidazole-type nitrogen (N3 and N7) of guanine (G) and the phosphate-sugar backbone can both contribute to the coordination interactions in Co-G₁₀. However, G is practically insoluble in DMF, and thus couldn't generate the self-assembly nanostructures in this synthesis condition.

(3) Only N3 in the pyrimidine base cytosine (C) has lone-pair electrons to coordinate with metal ions, because the N1 with -H group make itself an inefficient bonding site. Hence, free C molecule can't form Co-C assemblies with Co(II). However, in stark contrast to free C, the -R group (R is the phosphate-sugar backbone) in C₁₀ can donate additional bonding sites (e.g., phosphate O atoms), which in

combination with N3, can provide at least two bonding sites for the generation of Co-C₁₀ assemblies by the coordination interactions. Thus, Co-C₁₀ assemblies can be obtained in our experiments.

(4) Obviously, both N1 and N3 in T molecule are inefficient bonding sites to coordinate with metal ions. Thus, free T molecule can't form Co-T assemblies with Co(II). Although -R groups in T₁₀ might provide additional bonding sites, the Co-T₁₀ assemblies were still not formed in our experiment, indicating that there are very limited coordination sites in -R groups (phosphate backbones and sugars).

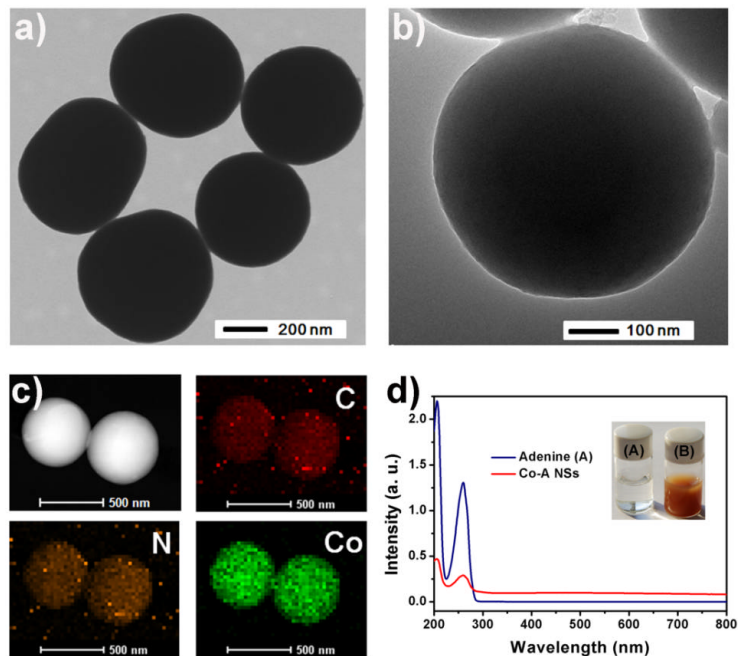


Figure S7. (a-b) TEM images of Co-A NSs. (c) HAADF-STEM and corresponding EDX elemental mapping images of Co-A NSs. (d) UV-vis absorption spectra of adenine and Co-A NSs. Inset: photograph showing the dispersibility of (A) adenine and (B) Co-A NSs in water.

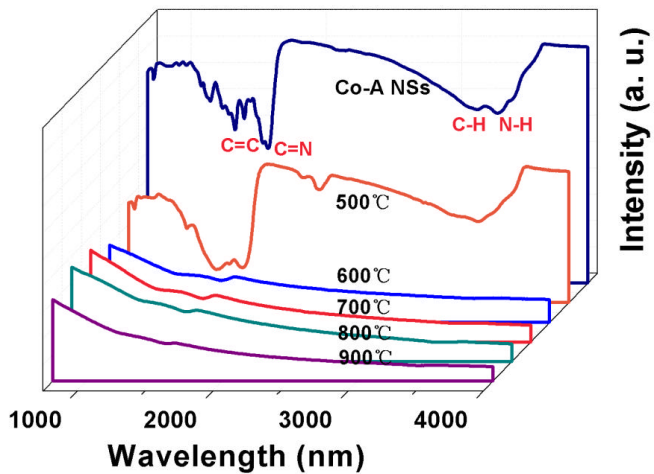


Figure S8. FTIR spectra of Co-A NSs and the pyrolysis products at different temperatures.

The FTIR spectrum of Co-A NSs indicates the characteristic absorption bands at $3000\text{-}3500\text{ cm}^{-1}$, which correspond to C-H and N-H stretching vibrations. Additionally, the skeleton stretching vibrations of heterocyclic adenine base with the absorption peaks at $1200\text{-}1600\text{ cm}^{-1}$ can be clearly identified. The FTIR spectrum of Co-A-500 is similar to that of the Co-A NSs precursor, demonstrating the largely preserved coordination structure. After pyrolysis of Co-A NSs at increased temperatures, the characteristic peak for C=N bonding (approximately 1600 cm^{-1}) can be observed, and the intensities of other characteristic peaks are decreased to a large extent.

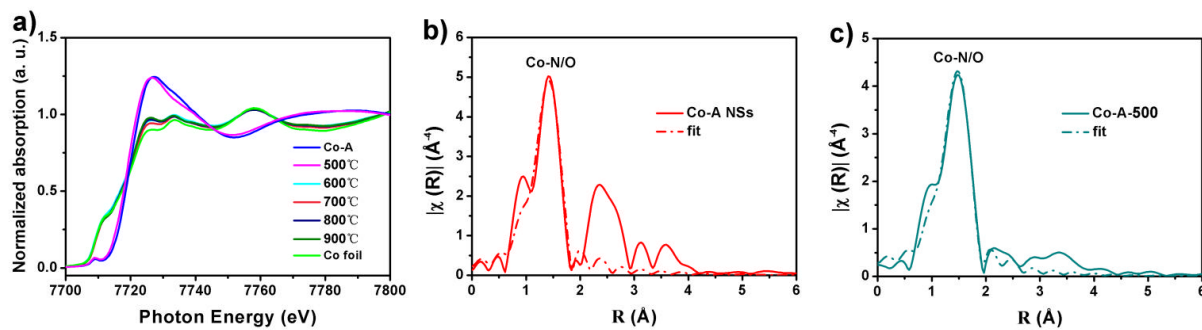


Figure S9. (a) Co K-edge XANES spectra for Co foil, Co-A NSs and the pyrolysis products at different temperatures. Observed (solid line) and calculated (dash line) Fourier transforms of k^3 -weighted Co K-edge EXAFS spectra for (b) Co-A NSs and (c) Co-A-500.

Nearly identical XANES spectra for Co-A and Co-A-500 prove that the majority of Co remains in the +2 oxidation state and the coordination structure is intact in Co-A-500. At higher activation temperatures (from 600 °C to 900 °C), the XANES spectra reveal extensive reduction of Co^{2+} to metallic cobalt, with its characteristic 1s – 4p transition at the energy of 7726 eV. However, an obvious increase in the white line intensity is observed for Co-N/C-x compared to the Co foil, highly indicating the distinctive nano-confined environment of Co-N/C-x.

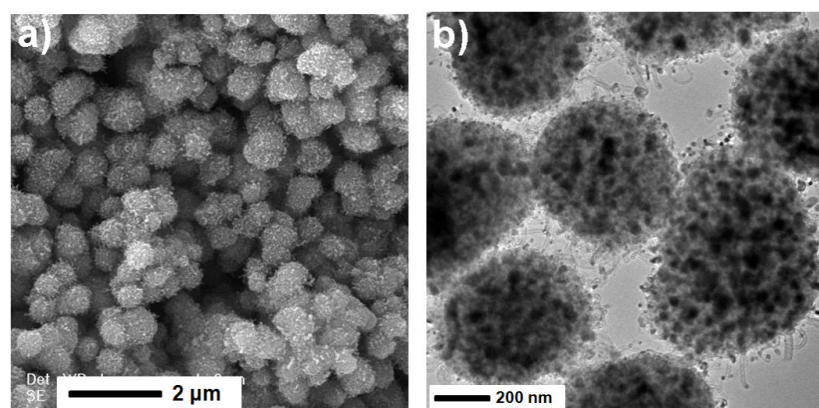


Figure S10. (a) SEM and (b) TEM images of rambutan-like Co-N/C-700.

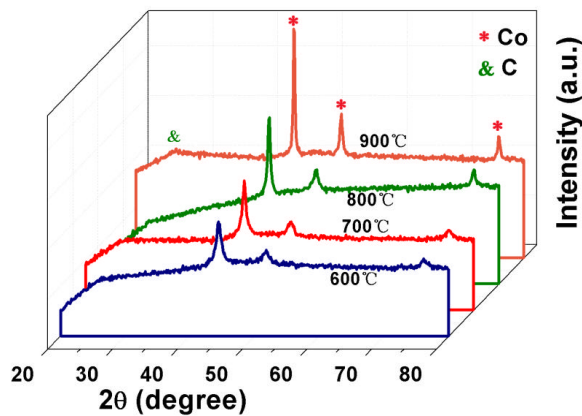


Figure S11. XRD patterns of Co-A NSs after pyrolysis at different temperatures.

The broad peak of the XRD pattern at about 26.5° corresponds to the (002) planes of the graphitic carbon, while the other sharp diffraction peaks are characteristic of metallic cobalt with a cubic phase (JCPDS 15-0806). It can be seen from XRD patterns that the high pyrolysis temperature is favorable for the formation of well-crystallized cobalt metal. At the same time, the diffraction peaks corresponding to graphitic carbon are observed to be quite broad and weak in the patterns because of its low amount and relatively low diffraction intensity.

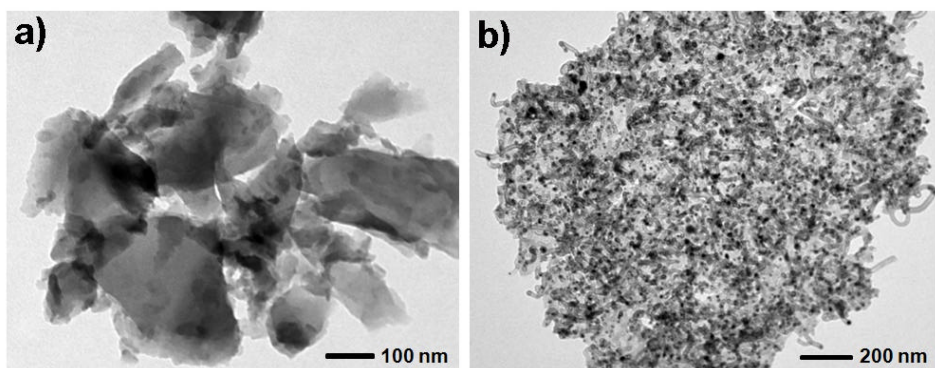


Figure S12. TEM images of (a) NC-A derived from the pyrolysis of adenine, and (b) Co/N/C derived from the pyrolysis of physically mixed adenine and cobalt nitrate.

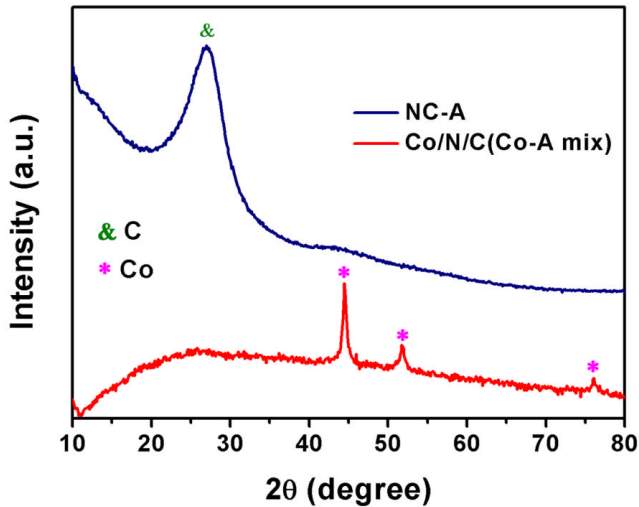


Figure S13. XRD patterns of NC-A derived from the pyrolysis of adenine, and Co/N/C derived by the physical-mixture method.

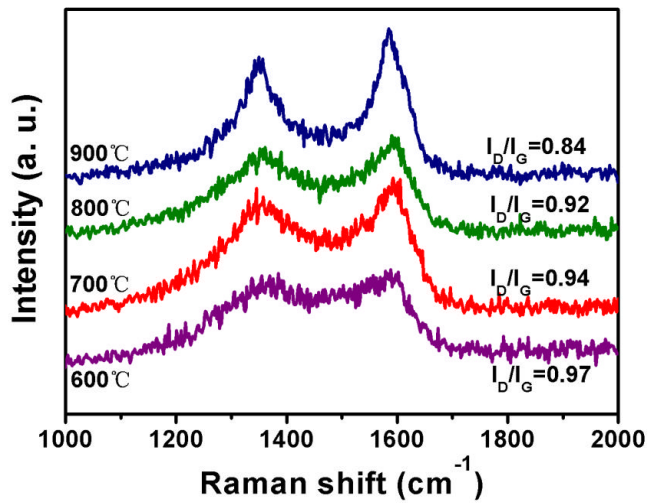


Figure S14. Raman spectra of the Co-N/C-x (x varies from 600 °C to 900 °C).

Raman data confirm the gradual change of local structure towards ordered graphitic carbon at increased pyrolysis temperatures [1].

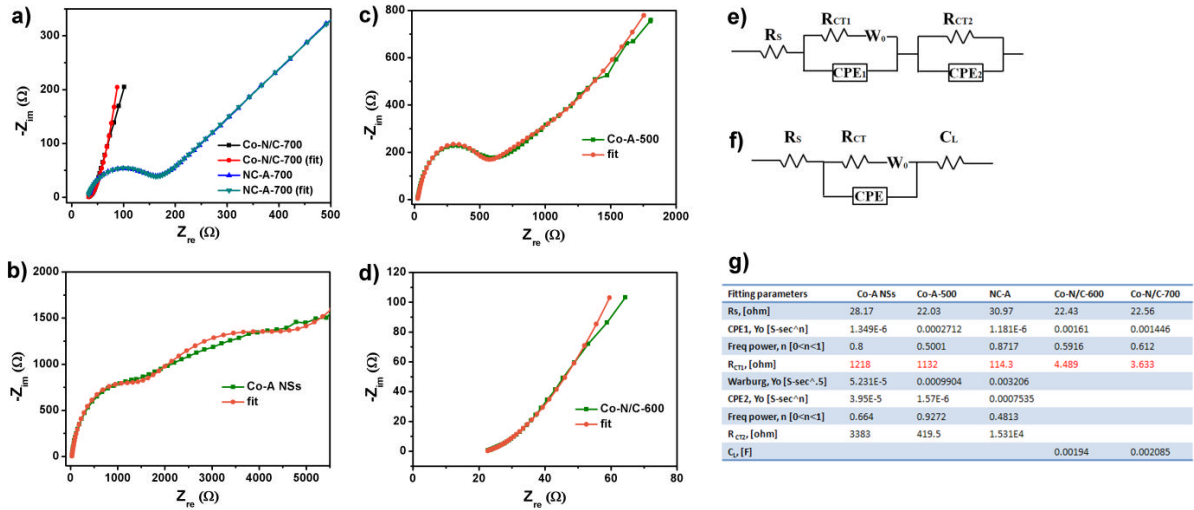


Figure S15. Nyquist plots of (a) Co-N/C-700 and NC-A-700, (b) Co-A NSs, (c) Co-A-500 and (d) Co-N/C-600, as well as their corresponding fitting plots calculated by using the software ZSIMPPWIN. (e) The electrical equivalent circuit used for fitting the impedance spectra of Co-A NSs, Co-A-500 and NC-A-700. (f) The electrical equivalent circuit used for fitting the impedance spectra of Co-N/C-600 and Co-N/C-700. (g) Equivalent circuit parameters obtained from the fitting results.

According to the equivalent circuit parameters obtained from the fitting results, the charge transfer resistance (R_{CT}) of Co-N/C-700 (3.6 Ω) is much lower than that of NC-A-700 (114 Ω) and Co-A NSs (1218 Ω). It is evident that the formation of MWCNTs and encapsulated metallic cobalt during the pyrolysis can concertedly enhance the electroconductivity of Co-N/C as compared to either NC-A or Co-A NSs precursor.

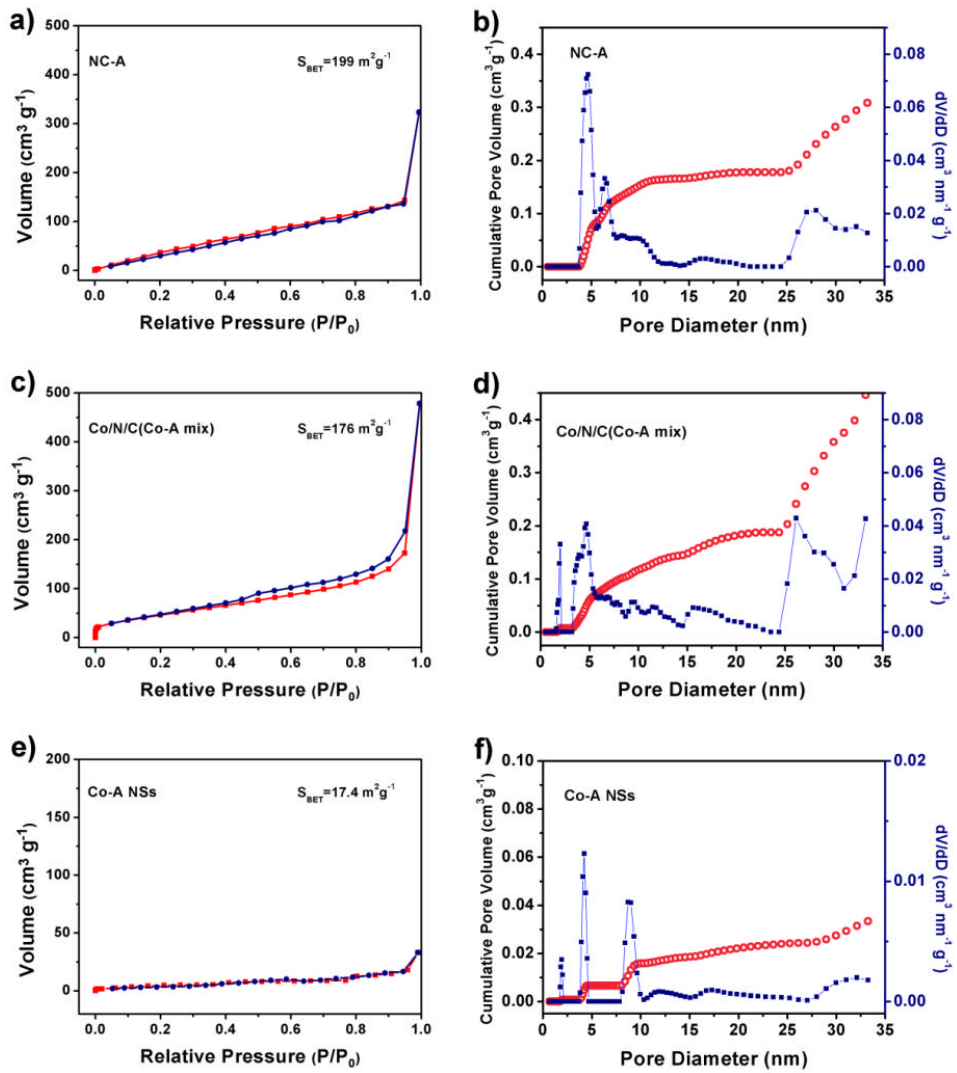


Figure S16. (a, c, e) N₂ adsorption-desorption isotherms and (b, d, f) the cumulative pore volume and pore-size distribution curves for (a-b) NC-A, (c-d) Co/N/C derived by physical-mixture method and (e-f) Co-A NSs.

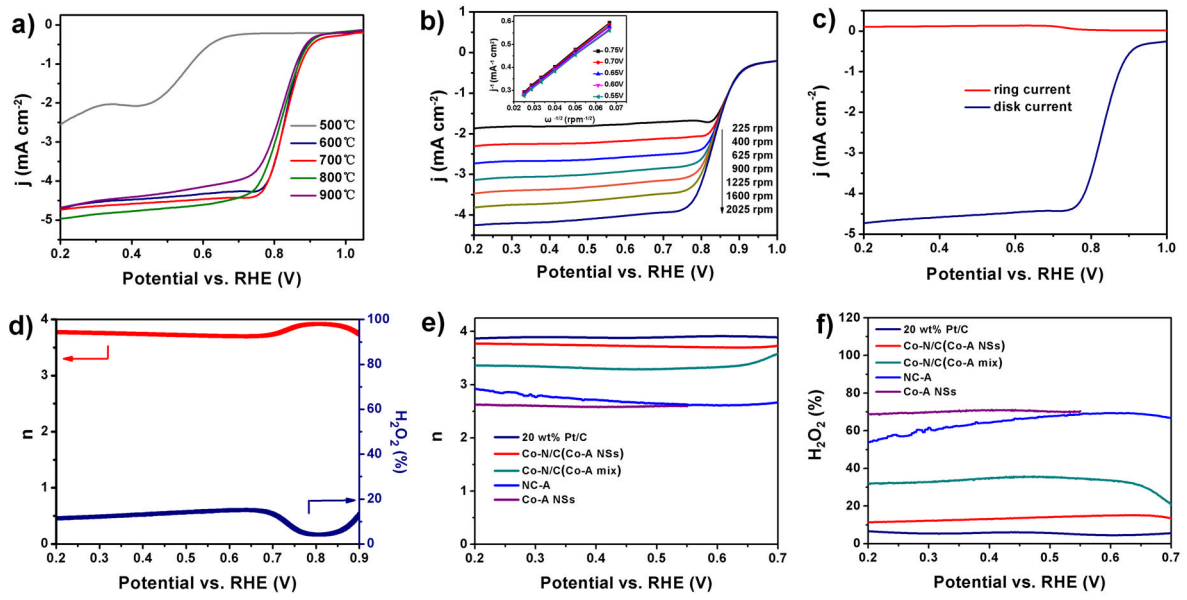


Figure S17. (a) Polarization plots of Co-A-x (x is the pyrolysis temperature that varies from 500 °C to 900 °C) in O₂-saturated 0.1 M KOH (1600 rpm). (b) Polarization curves of Co-N/C at different rotating speeds in O₂-saturated 0.1 M KOH. The inset in (b) is the corresponding Koutecky-Levich plots at different potentials derived from RDE. (c) The disk current and ring current of Co-N/C-700 at 1600 rpm in O₂-saturated 0.1 M KOH. (d) The electron transfer number (n) and peroxide yield of Co-N/C-700 at different potentials in O₂-saturated 0.1 M KOH. (e,f) The electron transfer number (n) and peroxide yield of various samples at different potentials in O₂-saturated 0.1 M KOH.

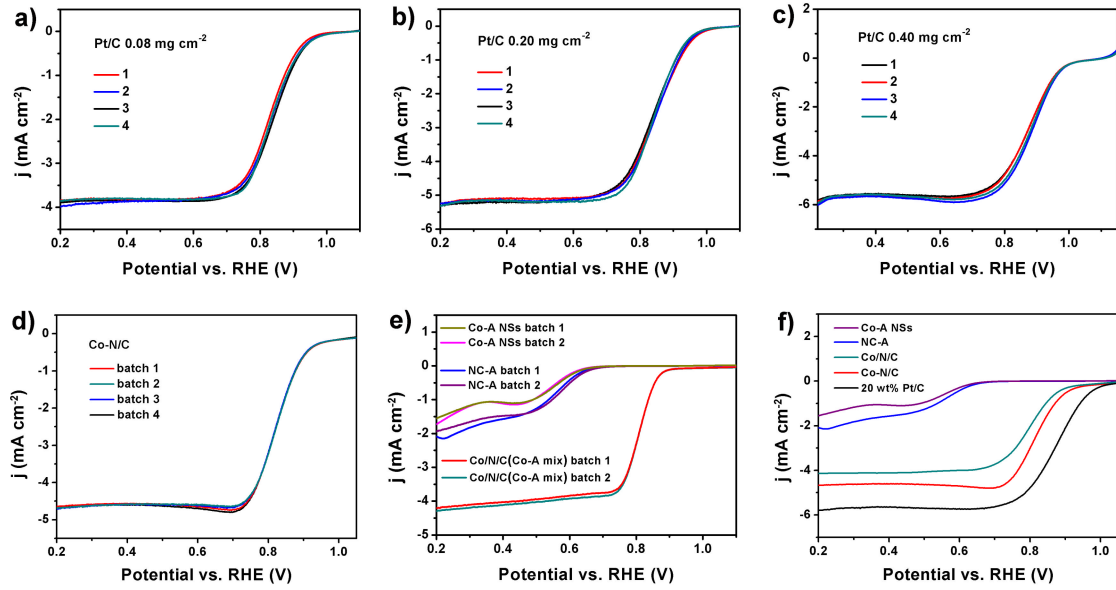


Figure S18. (a-c) The reproducibility of polarization curves at 1600 rpm for 20 wt% Pt/C with different loadings in O₂-saturated 0.1 M KOH. (d) Polarization curves at 1600 rpm for four batches of Co-N/C in O₂-saturated 0.1 M KOH. (e) Polarization curves at 1600 rpm for several batches of Co-A NSs, NC-A and Co/N/C in O₂-saturated 0.1 M KOH. (f) Polarization curves at 1600 rpm in O₂-saturated 0.1 M KOH for various samples. All non-precious catalysts and 20 wt% Pt/C loadings in (d-f) are 0.4 mg cm^{-2} .

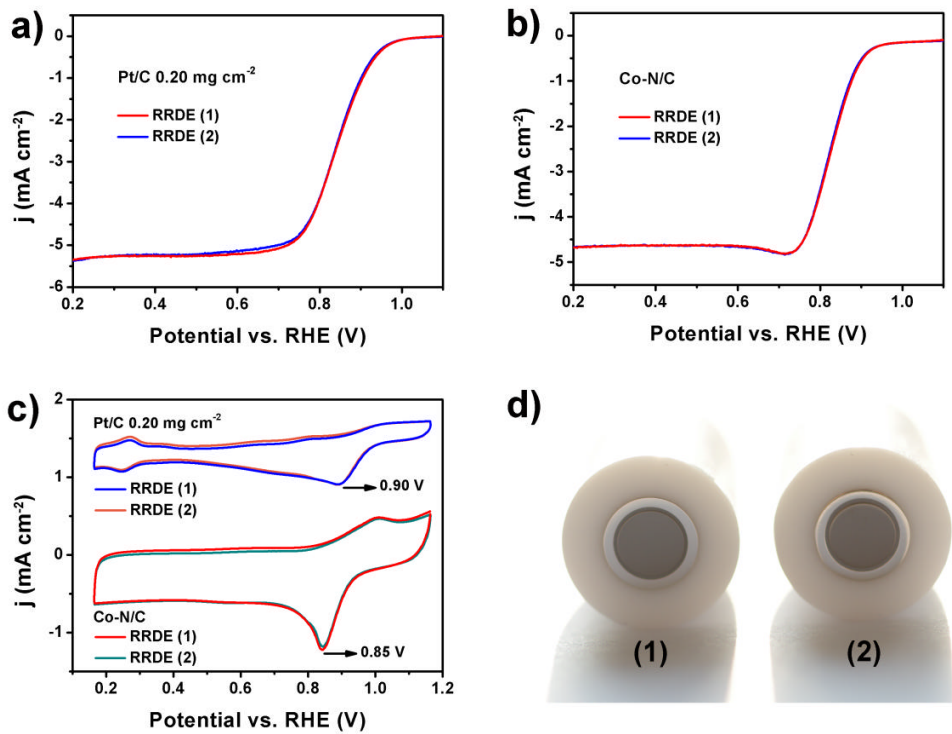


Figure S19. Polarization curves at 1600 rpm for (a) 20 wt% Pt/C and (b) Co-N/C in O_2 -saturated 0.1 M KOH with two RRDEs as the working electrodes. (c) CV curves for 20 wt% Pt/C and Co-N/C in O_2 -saturated 0.1 M KOH with two RRDEs as the working electrodes. (d) Photograph of the two RRDEs (both are 5.0 mm in diameter). The polarization curves and CV curves for either Co-N/C or 20 wt% Pt/C present almost identical results on the two RRDEs, which implies the proper reproducibility of the catalytic tests.

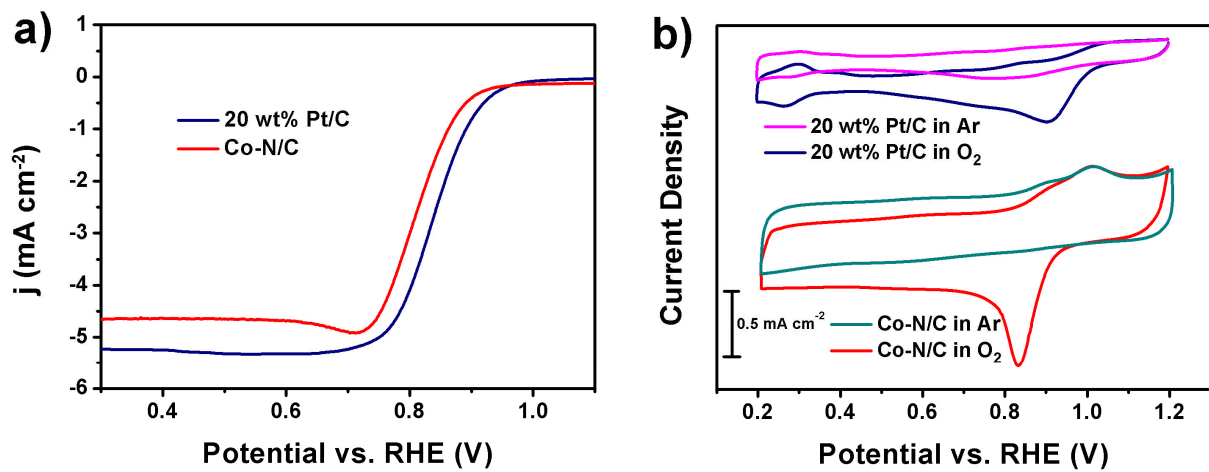


Figure S20. (a) Polarization curves at 1600 rpm and (b) CV curves for 20 wt% Pt/C and Co-N/C in O₂-saturated 0.1 M KOH. The ORR test employs a Pt disk as the counter electrode and an Hg/HgO electrode as the reference electrode. Co-N/C loading is 0.4 mg cm^{-2} ; 20 wt% Pt/C loading is 0.2 mg cm^{-2} .

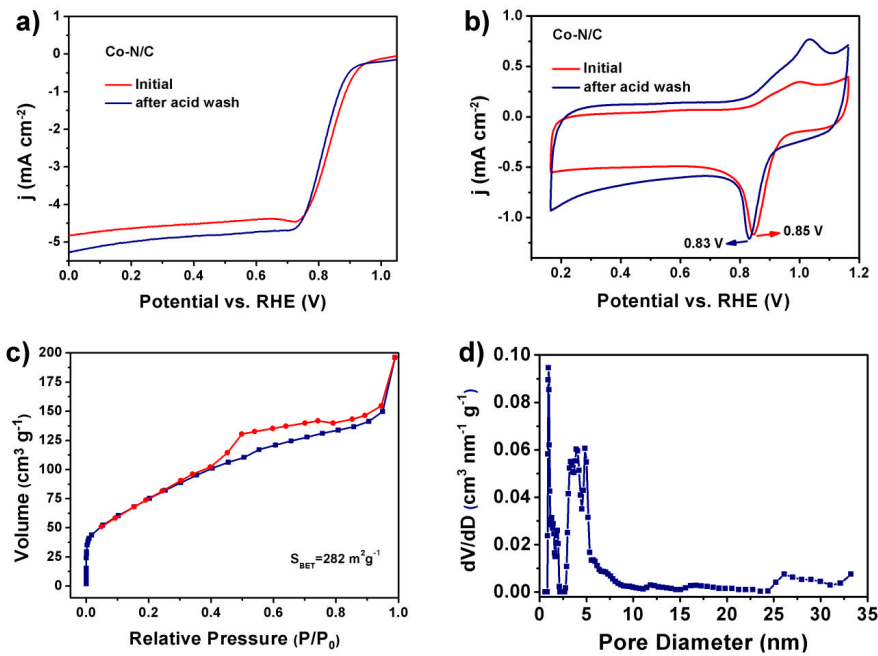


Figure S21. (a) Polarization curves at 1600 rpm and (b) CV curves in O₂-saturated 0.1 M KOH for Co-N/C catalyst before and after acid leaching in 0.5 M H₂SO₄ overnight. (c) N₂ adsorption-desorption isotherms and (d) the pore-size distribution curves for the acid-treated Co-N/C.

Compared with the untreated sample, the Co-N/C with acid washing exhibited a higher diffusion-limiting current density in the polarization curve and a higher area in the CV curve. Based on the ICP analysis, acid washing caused a weight loss of 26.4% Co. Additionally, due to the removal of the exposed small Co metal that has blocked the micropores, the acid-treated Co-N/C exhibited an increase in its S_{BET} (282 cm² g⁻¹) and a decrease in its average pore diameter (4.3 nm). Therefore, with the improved microporosity, the current density enhancement could be attributed to the more efficient mass transport. However, acid leaching of the Co-N/C could remove some inactive metal residues and unstable Co-N species. At the same time, this washing process resulted in contaminants in the catalyst. The dissolution and contamination of the active sites made the catalyst less active than the untreated sample in terms of the negative shift of the onset potential and CV peak potential. Therefore, Co-N/C catalysts were not acid-treated when applied in the electrocatalysis tests in alkaline condition.

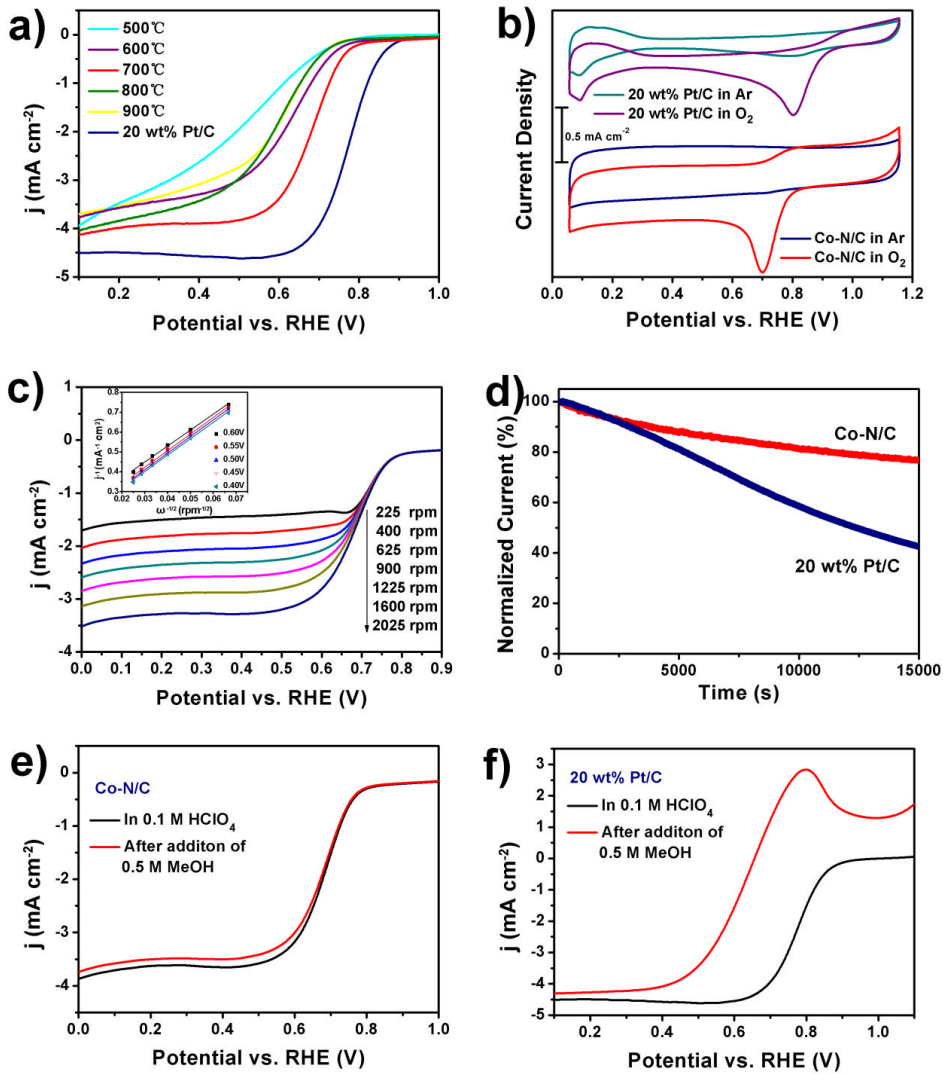


Figure S22. (a) Polarization plots for 20 wt% Pt/C and Co-A-x (x is the pyrolysis temperature that varies from 500 °C to 900 °C) in O₂-saturated 0.1 M HClO₄ (1600 rpm). (b) CV curves of Co-N/C-700 and 20 wt% Pt/C in Ar and O₂-saturated 0.1 M HClO₄. (c) Polarization curves of Co-N/C-700 at different rotating speeds. The inset in (c) represents Koutecky-Levich plots at different potentials derived from RDE. (d) Chronoamperometry (i-t) measurements of Co-N/C-700 and 20 wt% Pt/C in O₂-saturated 0.1 M HClO₄ at 0.65 V (vs. RHE), 225 rpm. (e,f) Polarization curves of Co-N/C-700 and 20 wt% Pt/C in O₂-saturated 0.1 M HClO₄ before and after addition of 0.5 M methanol, respectively. Note: Co-N/C catalyst samples were immersed in 0.5 M H₂SO₄ overnight and washed until neutral for further catalytic use. Co-N/C loading is 0.4 mg cm⁻²; 20 wt% Pt/C loading is 0.2 mg cm⁻².

The CV and RRDE measurements verify that Co-N/C-700 presents favorable ORR activity in the acidic condition. Moreover, due to its superior catalytic selectivity and durability, Co-N/C could also work as the cathodic ORR catalyst in proton exchange membrane fuel cells (PEMFCs), which operate under harsh acidic conditions.

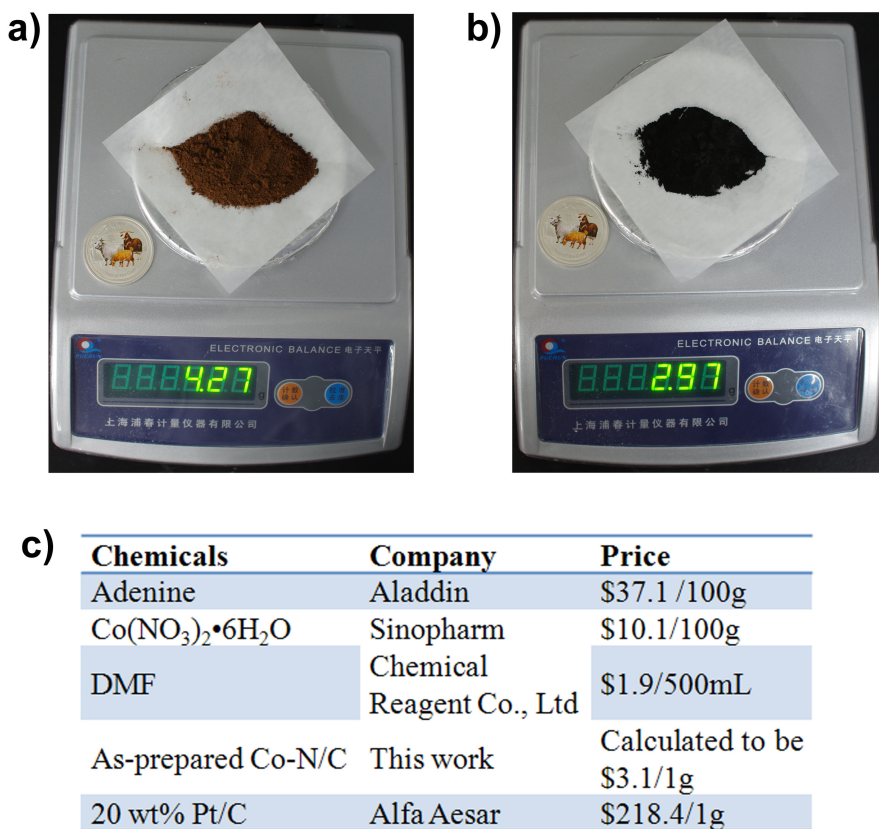


Figure S23. Large-scale production of (a) Co-A NSs and (b) the pyrolysis products Co-N/C. (c) The price of the raw-materials, the as-prepared Co-N/C and the commercial 20 wt% Pt/C.

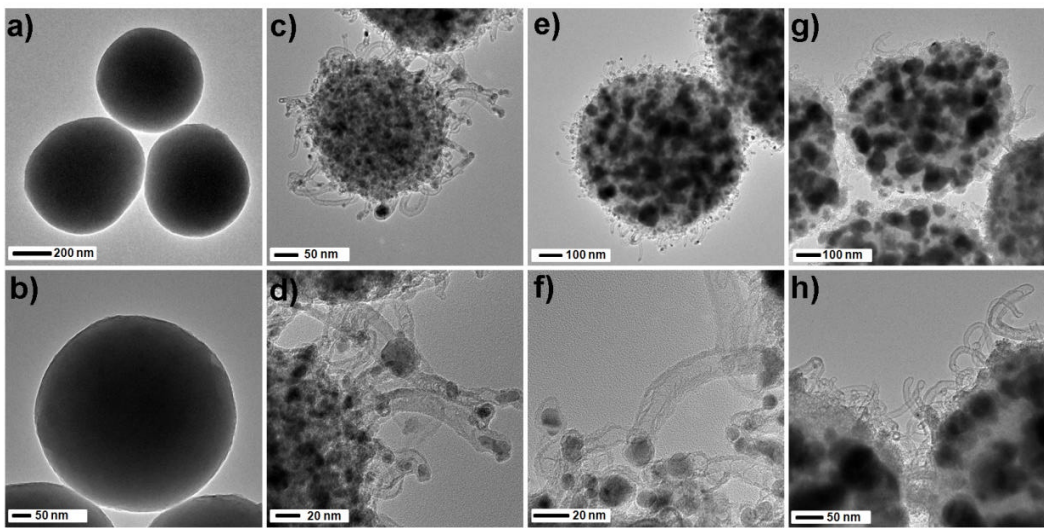


Figure S24. TEM images of Co-A NSs after pyrolysis at (a-b) 500 °C, (c-d) 600 °C, (e-f) 800 °C and (g-h) 900 °C.

TEM observations reveal that the as-prepared product remains spherical in shape after pyrolysis at 500 °C. The MWCNTs extruding out of the spheres began to appear at the temperatures above 600 °C. By pyrolyzing Co-A NSs at higher temperatures (800 °C and 900 °C), we noticed that larger aggregated Co particles were generated inside the porous spheres.

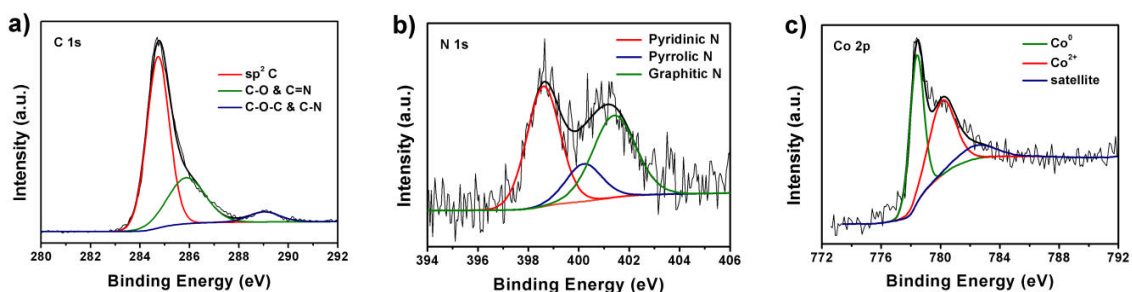


Figure S25. High-resolution (a) C 1s, (b) N 1s and (c) Co 2p XPS spectra of Co/N/C derived by physical-mixture method.

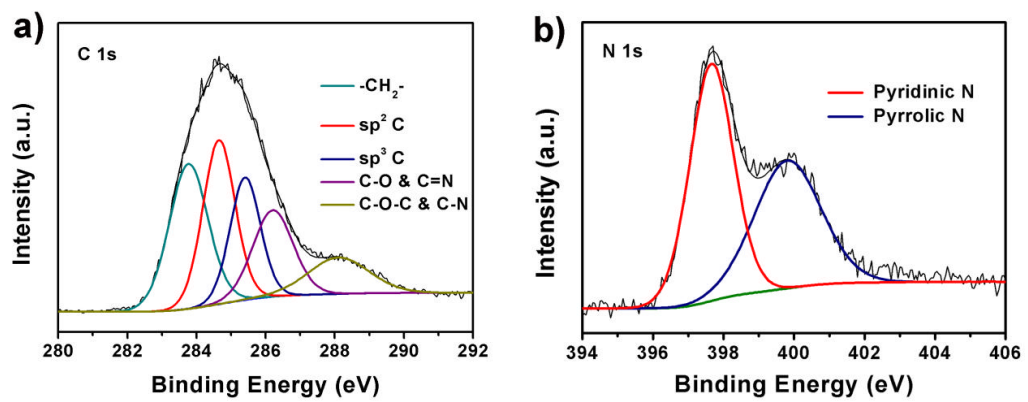


Figure S26. High-resolution (a) C 1s and (b) N 1s XPS spectra of NC-A.

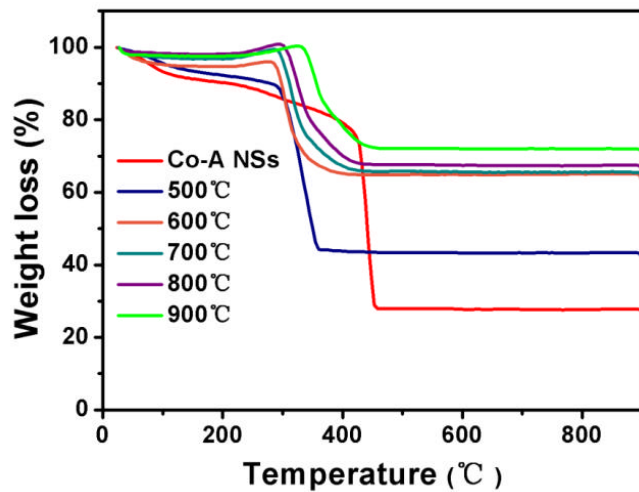


Figure S27. Thermogravimetric analysis (TGA) spectra in air atmosphere of Co-A NSs and the pyrolysis products at different temperatures.

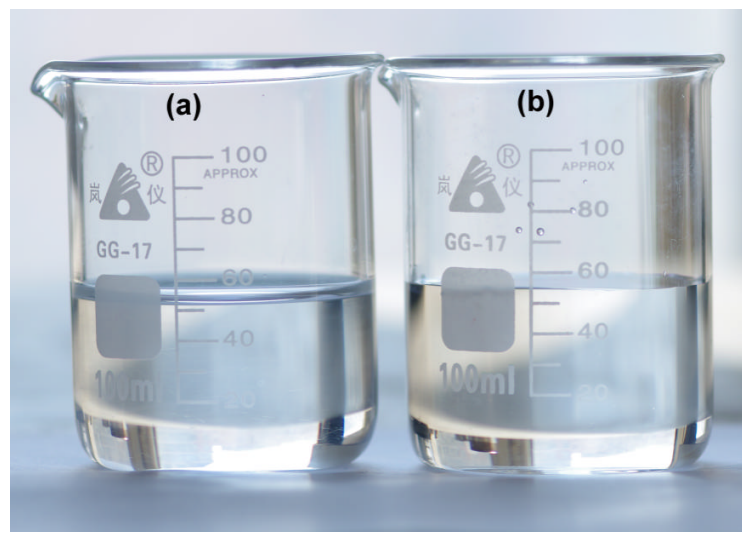


Figure S28. (a) 0.1 M KOH solution. (b) 0.1 M KOH solution after 10 000 times ORR cycles for Co-N/C. After 10 000 cycles, the separated supernatant of 0.1 M KOH electrolyte was analyzed by ICP-MS system, and the result displayed that no Co ion was detected in the electrolyte solution. The photographs show that the KOH electrolyte has no color change after 10 000 times ORR cycles for Co-N/C.

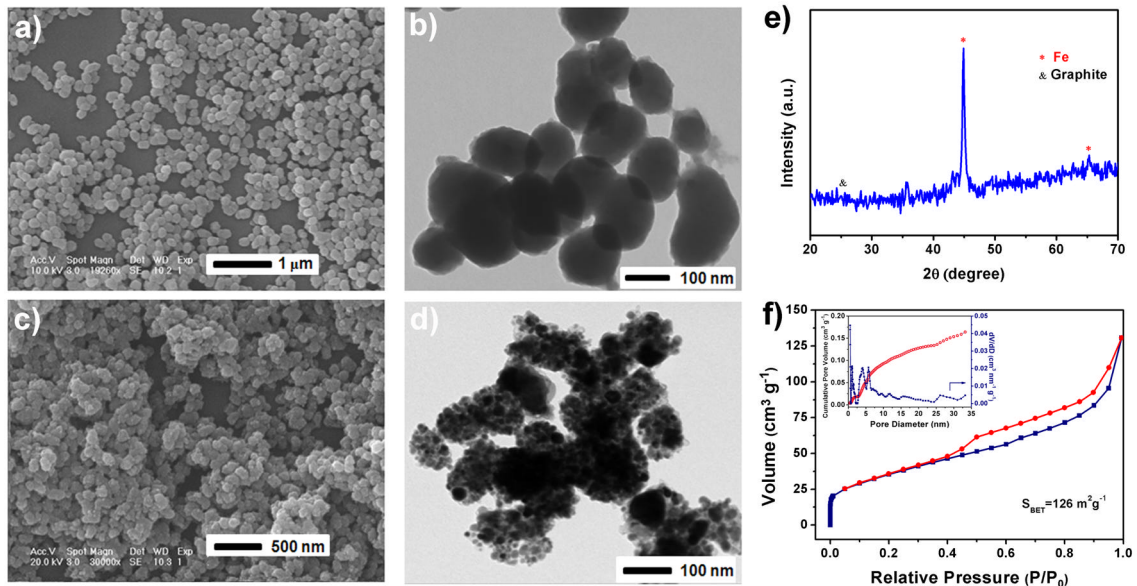


Figure S29. (a) SEM and (b) TEM image of Fe-A nanocomposites spheres. (c) SEM and (d) TEM image of Fe-N/C. (e) XRD pattern of Fe-N/C. (f) N₂ adsorption-desorption isotherms of Fe-N/C. The inset in (f) shows the cumulative pore volume and pore-size distribution curve.

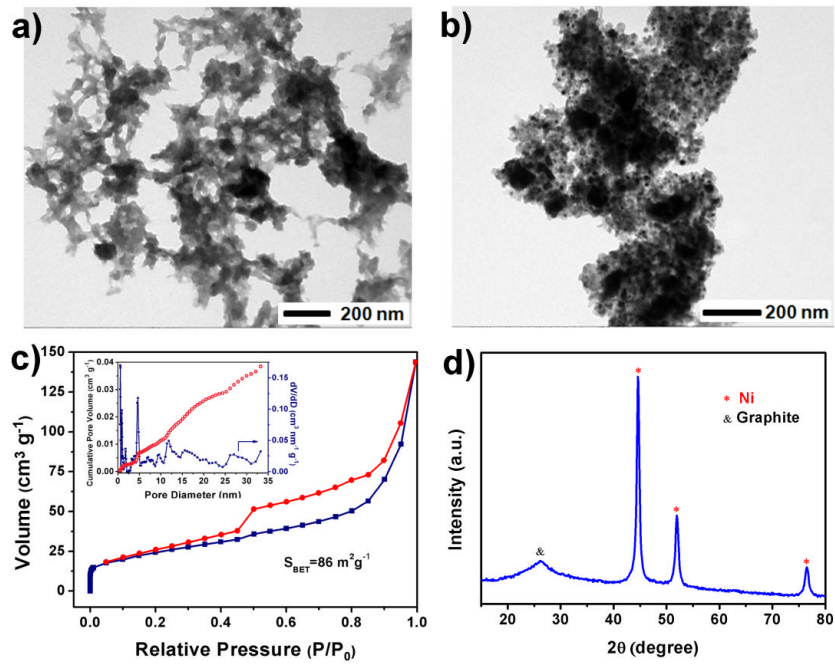


Figure S30. (a) TEM image of Ni-A nanocomposites. (b) TEM image, (c) N_2 adsorption-desorption isotherms and (d) XRD pattern of Ni-N/C. The inset in (c) shows the cumulative pore volume and pore-size distribution curve.

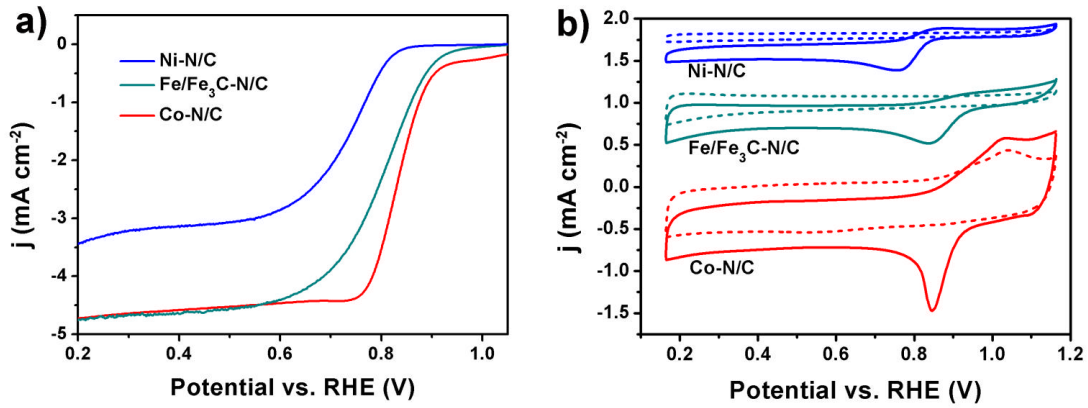


Figure S31. (a) Polarization curves at 1600 rpm and (b) CV curves in O_2 -saturated (solid line) and Ar-saturated (dash line) 0.1 M KOH for Co-N/C, Fe-N/C and Ni-N/C.

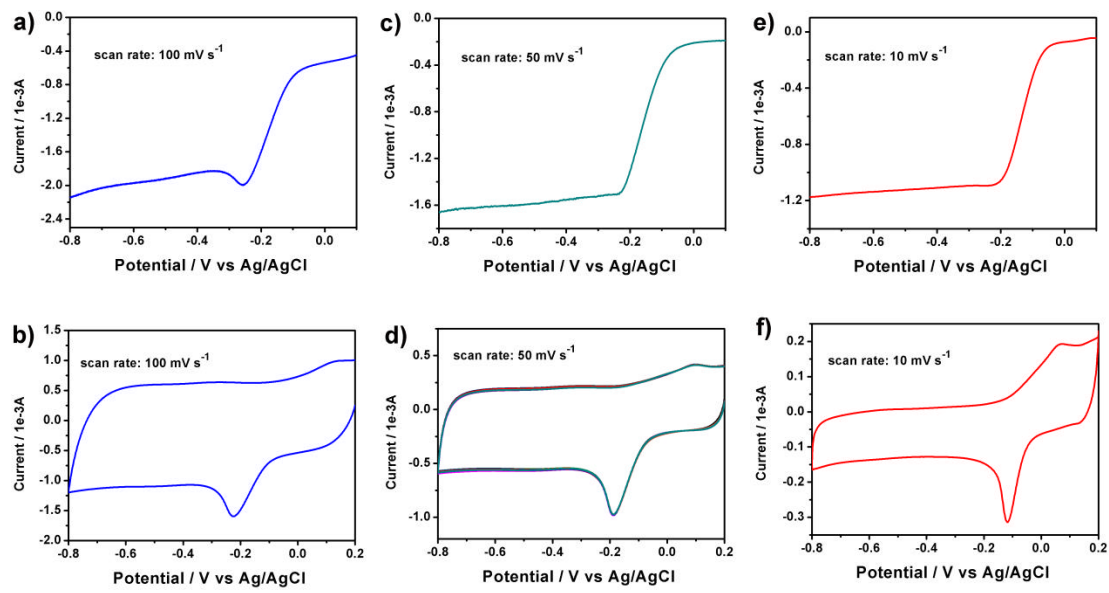


Figure S32. (a) Polarization curve and (b) CV curve of Co-N/C in O₂-saturated 0.1 M KOH at a scan rate of 100 mV s⁻¹. (c) Polarization curve of Co-N/C in O₂-saturated 0.1 M KOH at a scan rate of 50 mV s⁻¹. (d) Contiguous CV cyclic scans at a scan rate of 50 mV s⁻¹ for 20 times. (e) Polarization curve and (f) CV curve of Co-N/C in O₂-saturated 0.1 M KOH at a scan rate of 10 mV s⁻¹.

Table S1. Structural parameters extracted from quantitative EXAFS curve-fitting for Co-N/O in different samples.

Samples	R (Å)	CN	σ^2	E (eV)	R-factor
Co-A ₁₀	2.04	6.3	0.015	2.1	0.013
Co-G ₁₀	2.05	5.6	0.011	1.1	0.008
Co-C ₁₀	2.04	5.5	0.010	1.0	0.005
Co-A NSS	1.91	3.7	0.008	6.0	0.022
Co-A-500	1.97	3.7	0.010	1.4	0.009

R(Å): inter-atomic distance, CN: coordination number, σ^2 : mean-square relative displacement (Debye-Waller factor), E: shift of E_0 value, R-factor is a measure of the misfit distribution over both data sets (%).

Note: the N and O atoms are not distinguishable by this technique due to their close proximity.

Table S2. Summary of elemental contents in the as-prepared samples. C (wt%) and N (wt%) are from the quantitative elemental analysis, and Co (wt%) is from the detection of TGA.

Samples	C (wt%)	N (wt%)	Co (wt%)	N/C ratio (at%)	Co/C ratio (at%)
Co-A NSs	29.4	30.6	20.4	89.2	14.1
Co-A-500	25.5	26.8	31.8	90.1	25.4
Co-A-600	36.2	5.4	47.8	12.8	26.9
Co-A-700	40.9	3.9	48.1	8.2	23.9
Co-A-800	41.8	2.8	49.5	5.7	24.1
Co-A-900	41.2	1.7	52.8	3.5	26.1
NC-A	52.6	37.2	---	60.6	---
Co/N/C(Co-A mix)	36.9	2.7	56.2	6.3	31.0

Table S3. ORR catalytic activities of Co-N/C-700 compared to previously reported NPMCs materials in 0.1 M KOH.

Materials	Loading (mg cm ⁻²)	E _{onset} (V vs.RHE)	E _{1/2} (V vs.RHE)	Limiting current density (mA cm ⁻²)	Cathodic ORR peak (V vs.RHE)	Reference
Co-N/C-700	0.4	0.94	0.84	4.73	0.85	This work
Co-N-GN	0.1	0.87	0.80	4.12	0.78	[2a]
Co-g-C ₃ N ₄ @rGO	0.283	0.93	0.82	~4.50	0.81	[2b]
G-Co/CoO		~0.88	0.79	~4.50	0.77	[2c]
CoP-CMP800	0.6	0.84	0.78	4.62	0.73	[2d]
Fe-N/C-700	0.03	0.91	0.79	4.70	0.81	[2e]
Fe-N/C-800	0.1	0.92	0.81	6.06	0.85	[1b]

Table S4. ORR catalytic activities of 20 wt% Pt/C with different loadings on RRDE.

20 wt% Pt/C loading (mg cm ⁻²)	E _{onset} (V vs. RHE)	E _{1/2} (V vs. RHE)	Limiting current density (mA cm ⁻²)
0.08	0.98	0.84	3.9
0.2	1.00	0.86	5.3
0.4	1.02	0.88	5.8

Table S5. ORR catalytic activity of Co-N/C-700 compared to previously reported NPMCs materials in acidic solutions.

Materials	Loading (mg cm ⁻²)	E _{onset} (V vs.RHE)	E _{1/2} (V vs.RHE)	Limiting current density (mA cm ⁻²)	Cathodic ORR peak (V vs.RHE)	Reference
Co-N/C-700 ^a	0.4	0.81	0.69	4.1	0.70	This work
Co-N/C-750 ^a	0.6	0.83	0.68	~4.0		[3a]
Fe-N-HCMS ^b	0.5	0.80		6.8	0.60	[3b]
Fe-N-GC-900 ^a	0.6	0.88	0.74	5.3	0.71	[3c]
P _p PD-Fe-C ^b	0.9	0.83	0.72			[3d]
Fe-N/C-800 ^a	0.1	~0.80		6.1	0.69	[1b]
CoP-CMP800 ^b	0.6	0.74	0.64	4.8		[2d]

a: Tested in 0.1 M HClO₄; b: Tested in 0.5 M H₂SO₄.

Table S6. The catalytic performance of Co-N/C-700 compared to previously reported non-noble cathode catalysts materials used in the ADMFCs.

Cathode catalyst	OCV (V)	P _{max} (mW cm ⁻²)	Temperature (°C)	Loading amount (mg cm ⁻²)	Reference
Co-N/C-700	0.80	40.1	80	3	This work
GNPCSSs-800	0.71	33.8	80	4	[4a]
CNPs	0.81	22.7	60	3	[4b]
Fe ₃ C/NG-800	0.87	19	60	3	[4c]
BP-NFe	0.80	16.6	60	3	[4d]
BP-18F	0.70	15.6	60	3	[4e]
CB-NF	0.80	15.0	60	3	[4f]
NCNTs	0.33	7.4	25	4	[4g]
PAni-FeTsPc	0.65	6.0	20	5	[4h]

Note: OCV stands for the open-circuit voltage; P_{max} is the maximum power density.

Table S7. The relative percentage (%) of various configurations derived from the C 1s, N 1s and Co 2p XPS analysis in the as-prepared samples.

Samples	sp ² C	sp ³ C	Pyridinic N	Pyrrolic N	Graphitic N	Co ⁰	Co ²⁺
Co-A NSs	49.1	21.6	100	---	---	---	100
Co-A-500	52.6	20.4	100	---	---	---	100
Co-A-600	60.9	15.0	61.7	22.0	16.3	48.7	51.3
Co-A-700	71.9	---	52.0	21.8	26.2	45.1	54.9
Co-A-800	77.6	---	51.6	23.0	25.4	53.4	46.6
Co-A-900	77.5	---	41.4	17.5	41.1	51.3	48.7
NC-A	26.0	18.3	54.9	45.1	---	---	---
Co/N/C(Co-A mix)	65.1	---	45.1	15.2	39.7	51.1	48.9

Table S8. Porosity properties of Co-N/C-x based on N₂ physisorption.

Samples	BET surface area	Total pore volume
	(m ² g ⁻¹)	(cm ³ g ⁻¹)
Co-N/C-600	241.8	0.44
Co-N/C-700	253.2	0.57
Co-N/C-800	177.5	0.35
Co-N/C-900	136.8	0.36

References

- [1] a) J.-S. Lee, G. S. Park, S. T. Kim, M. Liu, J. Cho, *Angew. Chem. Int. Ed.* 52 (2013) 1026; b) L. Lin, Q. Zhu, A.-W. Xu, *J. Am. Chem. Soc.* 136 (2014) 11027.
- [2] a) S. Jiang, C. Zhu, S. Dong, *J. Mater. Chem. A* 1 (2013) 3593; b) Q. Liu, J. Zhang, *Langmuir* 29 (2013) 3821; c) S. Guo, S. Zhang, L. Wu, S. Sun, *Angew. Chem. Int. Ed.* 51 (2012) 11770; d) Z.-S. Wu, L. Chen, J. Liu, K. Parvez, H. Liang, J. Shu, H. Sachdev, R. Graf, X. Feng, K. Müllen, *Adv. Mater.* 26 (2014) 1450; e) A. Kong, B. Dong, X. Zhu, Y. Kong, J. Zhang, Y. Shan, *Chem. Eur. J.* 19 (2013) 16170.
- [3] a) S. Ma, G. A. Goenaga, A. V. Call, D.-J. Liu, *Chem. Eur. J.* 17 (2011) 2063; b) M. Zhou, C. Yang, K.-Y. Chan, *Adv. Energy Mater.*, DOI: 10.1002/aenm.201400840; c) A. Kong, X. Zhu, Z. Han, Y. Yu, Y. Zhang, B. Dong, Y. Shan, *ACS Catal.* 4 (2014) 1793; d) Y. Zhu, B. Zhang, X. Liu, D.-W. Wang, D. S. Su, *Angew. Chem. Int. Ed.* 53 (2014) 10673.
- [4] a) H. Zhong, J. Wang, Y. Zhang, W. Xu, W. Xing, D. Xu, Y. Zhang, X. Zhang, *Angew. Chem. Int. Ed.* 53 (2014) 14235; b) S. Zhao, H. Yin, L. Du, L. He, K. Zhao, L. Chang, G. Yin, H. Zhao, S. Liu, Z. Tang, *ACS Nano* 8 (2014) 12660; c) M. Xiao, J. Zhu, L. Feng, C. Liu, W. Xing, *Adv. Mater.* 27 (2015) 2521; d) J. Liu, X. Sun, P. Song, Y. Zhang, W. Xing, W. Xu, *Adv. Mater.* 25 (2013) 6879; e) X. Sun, Y. Zhang, P. Song, J. Pan, L. Zhuang, W. Xu, W. Xing, *ACS Catal.* 3 (2013) 1726; f) X. Sun, P. Song, Y. Zhang, C. Liu, W. Xu, W. Xing, *Sci. Rep.* 3 (2013) 2505; g) G. K. Goswami, R. Nandan, B. K. Barman, K. K. Nanda, *J. Mater. Chem. A* 1 (2013) 3133; h) S. Baranton, C. Coutanceau, J.-M. Léger, C. Roux, P. Capron, *Electrochim. Acta* 51 (2005) 517.